HiSST: 2nd International Conference on
High-Speed Vehicle Science & Technology
11–15 September 2022, Bruges, Belgium

Parametric Analysis of Performance of External Burning Ramjet using Hydrogen Injection in High-Speed Flow

Matus Cvengros[1], *Quentin Michalski*[1]

Abstract

External burning ramjet (EBR) is an interesting candidate for hypersonic airbreathing propulsion, presenting a unique application of supersonic combustion without the drawbacks of scramjets such as inlet unstart and choking. This research focuses on a parametric study of three-dimensional hydrogen injection in Mach 7.6 and Mach 11.4 flow and subsequent external burning in a wedge geometry using Computational Fluid Dynamics (CFD). The simulations employ detailed 13 species hydrogen-air chemistry model. Numerical results are compared to previous experimental study of a wedge-shaped external burning combustor. The performance of the configuration is subsequently assessed by varying the location of the injectors along the compression surface of the wedge and the injector fuel pressure. The results suggest that in all simulated cases, the combustion throughout the expansion fan is quenched mainly by the sudden temperature and pressure drop.

Keywords: *external burning ramjet, ramjet, scramjet, external burning, hydrogen injection*

Nomenclature

Latin

A – Surface area
C_L – Lift coefficient
C_D – Drag coefficient
I_{sp_A} – Axial specific impulse
I_{sp_N} – Normal specific impulse
M – Mach number
T – Static temperature
d – Injector diameter
k – Turbulent kinetic energy
$\dot{m}_i$ – Mass flow of associated with species i
p – Static pressure
u – Streamwise velocity
x – Axial position

Greek

α_i – Mass fraction of species i
η_m – Mixing efficiency
η_b – Burning efficiency
ρ – Density

Superscripts

r – Species mass fraction available for reaction
$*$ – All products of given species, including radicals

Subscripts

∞ – Freestream value
0 – Stagnation value

1. Introduction

Supersonic combustion is a key technology that could enable hypersonic airbreathing propulsion. Scramjets have received the most focus so far but still face challenging problems in order to achieve sustained operation. In a typical scramjet, the design needs to take into account various parts of the propulsion unit, including the engine forebody, supersonic inlet, isolator, combustion chamber and nozzle, such that high combustion efficiencies are achieved and unfavourable events such as inlet unstart are avoided. The design of the supersonic inlet in particular is a key element of a scramjet combustor design [1], as its purpose is to create the initial compression and conditions upstream of the combustor that will best promote the supersonic combustion process. On inappropriate designs, the operation of the combustor can result in adverse inlet-combustor interactions and cause an inlet unstart [2, 3]. An inlet unstart is characterised by an increase in pressure downstream of the inlet. This pressure increase travels up-

[1]*Royal Melbourne Institute of Technology.*

stream of the inlet and results in a highly unsteady flow spillage that can produce violent structural loads an order of magnitude larger than the steady-state loads [3, 4].

External Burning Ramjet (EBR) is another candidate of technology that could possibly enable supersonic combustion [5, 6] in hypersonic flight. In contrast to scramjets, an EBR consists of only the engine forebody and the expansion surface. The engine forebody serves as an inlet, as it is indistinguishable from the vehicle itself. The forebody shape also induce an oblique shock, behind which the adiabatic compression conditions enables the auto-ignition of the fuel-air mixture. The EBR does not rely on a cowled combustion chamber and the combustion process occurs at the surface of the vehicle open to the atmosphere. Therefore, unfavourable events such as inlet unstart can no longer occur and the engine design is simplified. Similar to scramjets, the engine aftbody serves the same purpose as a nozzle, and is responsible for accelerating the flow. In its most basic configuration, an EBR consists of only 2 geometric regions: (1) compression and (2) expansion surface [7]. The conceptual diagram of such configuration is shown in Fig. 1.

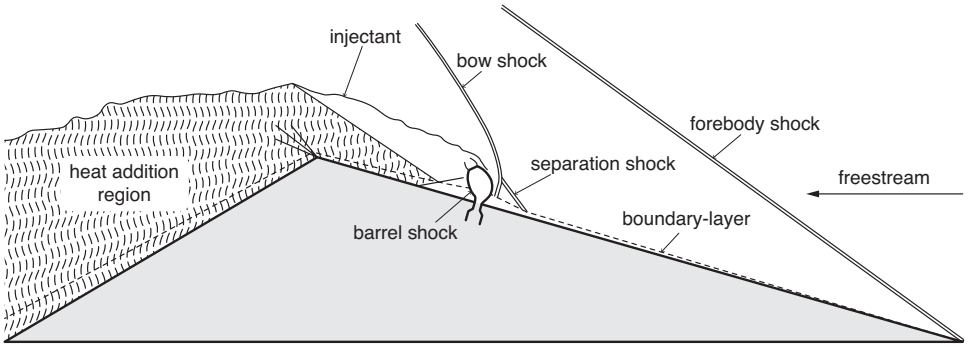

Fig 1. Diagram of an EBR. Location of fuel injection at the compression surface is schematically shown, together with the heat release associated with continuous burning of fuel at the expansion surface.

The fuel injection and mixing happens along the compression surface into the surrounding flow. The injection creates complex flow structures and flow properties characterised by displacement of the boundary-layer, development of shock regions and strong vortical structures downstream of the injector [8]. If the conditions of the flow are favourable and if the fuel is sufficiently mixed with oxygen from the surrounding flow, the formed fuel-air mixture ignites. The whole EBR concept relies on heat addition around the expansion/turning point ("knee"), effectively delaying the Prandtl-Mayer expansion [9, 10] and preserving the pressure on the expansion surface. The burning and addition of heat in the expansion region then has the potential to mitigate drag, create normal and lateral forces or even small amounts of thrust. Possible applications of the EBR could thus also include attitude control as well as propulsion.

Most of the studies of EBR available in the literature remain very conceptual and few actually address the physical implementation of the concept. Modelling the combustion as a heat addition process, it has been shown that the behaviour of EBR is strongly driven by the freestream conditions [11, 12] and geometry of the body [5, 6]. However, the influence of those parameters on the actual heat addition process has not been thoroughly addressed. To the author knowledge, the only experimental work that measured the pressure traces on compression and expansion surface with injection and combustion of hydrogen was that of Coras and Paull [7]. Jones and Christo [13] studied the same configuration numerically with injection of hydrogen and ethylene, however the injection conditions were not a close match to the experiment. In the same study, the experimental case with hydrogen is replicated and it is shown that most of the combustion process happens on the compression surface. In the works of Coras and Paull [7] and Jones and Christo [13], the hydrogen injection port was near the leading edge of the compression surface.

This work investigates the influence of the injector position at 3 different locations on the compression

ramp. The effects of the fuel mass flow as well as that of the flight Mach number are discussed. The study is conducted using fully three-dimensional CFD. Hydrogen is used as a fuel and its combustion process in air is fully resolved using detailed chemical kinetics. The geometry of computational cases is based on the reference case of Coras and Paull [7] and a reference case is compared against their experimental results. The impact of the studied parameters on the mixture formation, combustion process and resulting propulsion properties are then discussed and analysed.

2. Methodology

2.1. Numerical Domain

The geometry of the EBR studied is based on the experimental case of Coras and Paull [7]. The geometry is a long wedge (see Fig. 2b) with 5 separate injectors of diameter $d = 2$ mm positioned 13 mm downstream of the leading edge of the compression ramp.

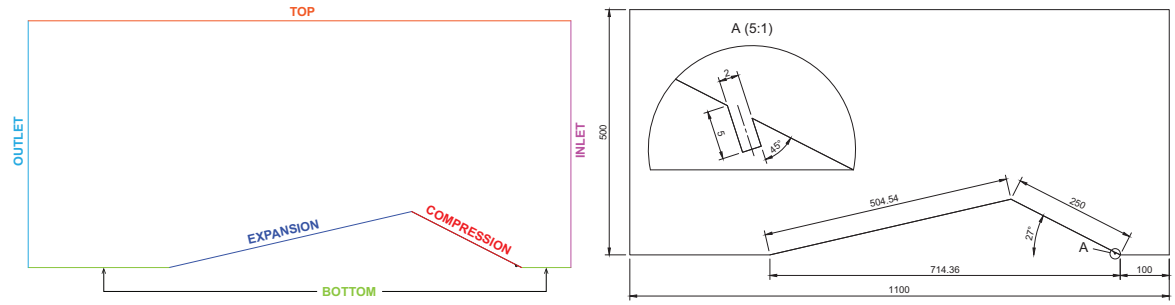

(a) Domain boundary conditions. **(b)** Configuration with the front injector.

Fig 2. Domain, boundary conditions and dimensions.

The compression ramp had a 27° angle and was chosen such that the flow behind the oblique shock produced by the ramp created sufficient conditions for the auto-ignition of the injected hydrogen fuel. Experiments [7] were conducted in the T4 shock tunnel at the University of Queensland. Non-reactive and reactive cases were studied using nitrogen and air atmosphere, respectively. The experimental pressure traces along the compression and expansion surface were retrieved using 1 mm pressure tap holes.

The numerical domain is 1100 mm long and 500 mm high (see Fig. 2a). In order to reduce the computational costs, the simulation domain of each grid is reduced by assuming a single-injector configuration cut in half through its symmetry plane (see Fig. 3a).

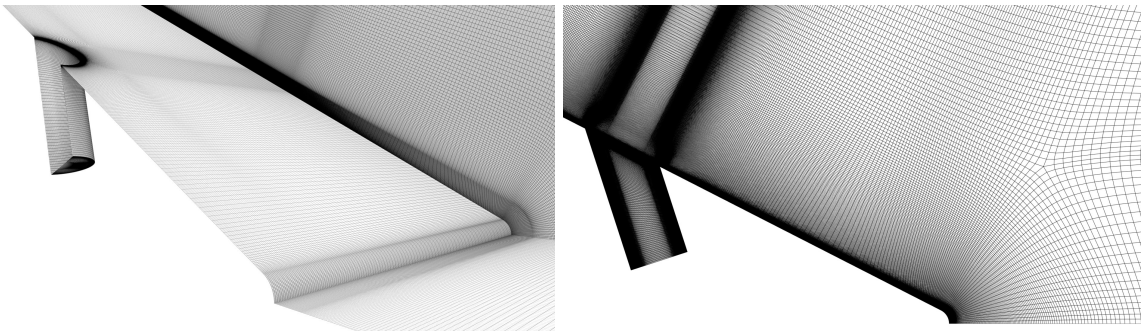

(a) Computational domain. **(b)** Grid topology near injector positioned 13 mm from the blunt leading edge of the compression ramp.

Fig 3. Computational domain and grid topology of the injector nearfield.

2.2. Numerical Methods

The flow field solutions are integrated using the commercial CFD++ solver. The solver used a Reynolds Averaged Navier-Stokes (RANS) turbulence modelling with the two-equation $k-\omega$ shear stress transport (SST) turbulence model [14]. The $k-\omega$ SST turbulence model was successfully used in studies of multi-porthole injector arrays with hydrogen fuel injection [8, 15]. Steady-state implicit backward Euler numerical scheme was used and the spatial discretisation was resolved using a three-dimensional second-order accurate total variation diminishing interpolation. The chemical reactions are solved using following the detailed mechanism of Jachimowsky (13-species, 33-reaction) [16]. The RANS solution in each run was deemed sufficiently converged if global residuals were reduced by at least 5 orders of magnitude.

The grids used in this work were generated with Pointwise (18.4R4). A total of 3 separate grids were constructed for 3 separate positions of injectors. Apart from the injector position, the grid features such as the resolution of the boundary-layer and cell density near the features of interest (ramp, injector, turning point) were preserved. Each grid consisted of approximately 23 million fully-structured hexahedral elements, constructed using a multi-block topology approach. The boundary-layer was fully resolved and employed at least 50 layers up to a height of approximately 14 mm, analytically predicted by turbulent boundary-layer thickness of flow over a flat-plate.

A particular attention was given to the model of the injection process and to the leading edge of the compression ramp to further increase the fidelity of the simulation compared to the experiment. The injector port is a small 4 mm (center-to-center) recessed round hole of 2 mm diameter (see Figure 2b).

Similar to the experimental case, it is inclined at 45 degrees relative to the compression surface so that on the injection surface the injector outlet is effectively elliptical. The recessed manifold was meshed to fully resolve the boundary-layer (see Figure 3b). All no-slip surfaces were resolved to $y^+ < 1$; this applies to the injector walls, the compression and the expansion surface. The leading edge of the compression ramp has a round radius of 0.5 mm and the turning point was modelled with the same radius (see Figure 3b). A supersonic flow condition is used at the outlet.

A grid convergence study was conducted for the same conditions as in the experimental configuration, however with varying cell density resulting in 3 separate grids: (1) coarse with 7 million, (2) medium with 23 million and (3) fine with 61 million cells. The grid convergence was assessed using the Grid Convergence Index (GCI) based on Richardson's extrapolation as described by Celik et al. [17]. The medium grid size was chosen for all simulations.

The simulations were performed using 960 CPU parallel cores on the National Computational Infrastructure (NCI) supercomputer at the Australian National University (ANU).

2.3. Parametric Space

The freestream static conditions are the same as in the experiments, the static pressure p_∞ is of 2.3 kPa and the static temperature T_∞ is of 302 K. The Mach number is a parameter of the study. The injector inlet conditions were prescribed using total pressure and total temperature. The total pressure value was initially set to match the mass flow conditions given in the experiments and was further a study parameter. Total temperature was set to 352 K and was also used as a parameter for certain cases. Coras and Paull [18] provide a total mass flow of hydrogen for all 5 injector of 18 g/s. This implies that for half of the injector inlet, the mass flow is of 1.8 g/s.

This study involves a parametric variation of three separate parameters: (1) the freestream conditions, (2) the injector position and (3) the total pressure of hydrogen at injector inlet. The freestream velocity was changed such that the Mach number varied between 7.6 and 11.4, where 11.4 is a 50 % increase from the nominal conditions. The injector pressure was varied from 0.95 MPa to 3.8 MPa and conditions were studied for three separate positions. The total temperature of the injected fuel was 352 K for all cases. The initial case given by Coras and Paull [7] had the injector located 13 mm from the tip of the leading edge (A), two additional locations are studied. The second configuration (C) is positioned 13 mm from the turning point; which corresponds to 237 mm from the leading edge. The third is set in between

location (A) and (C) at a distance of 135 mm from the leading edge.

A summary of the experimental simulation performed and their associated parameters is reported in Table 1.

Table 1. Parameter space and the test matrix.

Case ID	Inj. Pos.	Mach [–]	$p_{0_{H_2}}$ [MPa]	Reactions
A-7M6	A	7.6	N/A	No
A-11M4	A	11.4	N/A	No
A-7M6-BP-NR	A	7.6	1.9	No
A-7M6-BP-R	A	7.6	1.9	Yes
A-11M4-BP-NR	A	11.4	1.9	No
A-11M4-BP-R	A	11.4	1.9	Yes
A-11M4-HP-NR	A	11.4	3.8	No
A-11M4-HP-R	A	11.4	3.8	Yes
B-7M6-BP-NR	B	7.6	1.9	No
B-7M6-BP-R	B	7.6	1.9	Yes
C-7M6-BP-NR	C	7.6	1.9	No
C-7M6-BP-R	C	7.6	1.9	Yes
C-11M4-BP-NR	C	11.4	1.9	No
C-11M4-LP-NR	C	11.4	0.95	No
C-11M4-LP-R	C	11.4	0.95	Yes

3. Validation and Comparison with the Experiment

The cases **A-7M6-BP-NR** and **A-7M6-BP-R** are compared with the experiments of Coras and Paull [7]. In the experiments, the pressure data with and without hydrogen injection were recorded, and nitrogen gas was used in order to measure the effect of mass addition to surrounding flow without combustion. The pressure traces along the intersection curve of the compression and expansion surface at the position of symmetry plane were recorded and normalized by p_{0_∞}. The normalized pressure for both the non-reacting and reacting cases are compared to the experimental data (see Figure 4).

The experimental reactive case shows higher pressure on both the compression and expansion surfaces. The increase in pressure is the result of the heat addition process on both the compression and expansion surface. The combustion locally increases the static temperature which in turn reduces the Mach number and increases the static pressure. The comparison with the experimental results suggest a slight over-prediction of the static pressure for the compression region and a good match on the expansion surface. This comparison demonstrates that the current numerical method is able to capture the pressure rise in the expansion region associated with the combustion process. The compression surface discrepancy is more pronounced near the turning point. The experiment is run for a very short time and the pressure shows some fluctuations that the simulations do not account for.

Properties that result from the integration of the pressure over the surface are then compared to the experimental ones (see Table 2).

Table 2. Comparison of experimental and simulation specific impulse.

	I_{sp_N} [s]	I_{sp_A} [s]
Experiment	228	168
Simulation	1831	-368

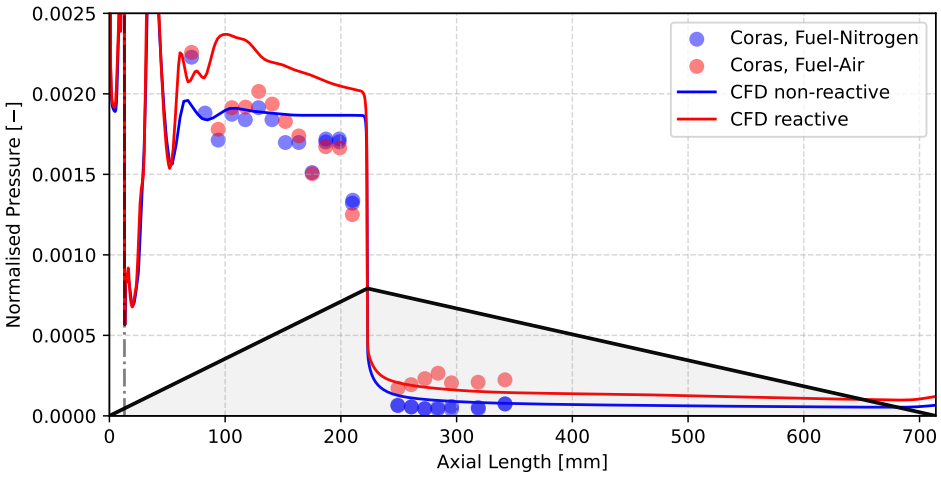

Fig 4. Comparison of pressure traces as normalised pressure. Both non-reactive and reactive datasets are compared. The vertical dashed line marks the position of the injector.

The axial and normal forces are calculated for both reactive and non-reactive case as well as for a reference case run without injection. The later case is then used to account for the effect of the flow on the model surface. The net force differences are computed as the difference between the injection and non-injection cases. The results thus account for either the effect of mass addition only (in the non-reactive cases) or the effect of mass addition with the combustion effect (in the reactive cases). Specific impulse can be derived for both the axial and normal force and is calculated as the net force divided by the product of the gravity constant and the total mass flow of injected fuel. The mass flow is measured at the injector inlet and only the hydrogen products are accounted for. In the experimental results of Coras and Paull [7], a positive normal specific impulse suggests net downward force and a positive axial specific impulse suggests net thrust. For the results presented in this paper, the convention presented in the experimental results is adopted. Therefore, a negative specific impulse suggests that a net drag is obtained.

Although the pressure traces through the center of the model are a good qualitative match, the resulting specific impulse differ quite a lot. In the experiments, the model is open on the sides which leads to possible additional pressure relief. This additional pressure relief might lead to spill over the sides that might strongly influence the overall forces applied on the model and possibly the combustion phenomena, particularly near the edges [7]. This process is clearly not correctly captured in the simulations. The effect could also explain that the simulation overestimate the pressure on the model at the compression surface. The experiment also predicts a positive net thrust, that although small, suggests the combustion might be happening much further away on the compression surface and also through the expansion fan.

The experimental case conditions are considered as the baseline for the parametric studies that are conducted in the rest of the work. In what follows, the tools for the analysis of the combustion and mixing process are introduced and applied to this reference point. The simulation domain is decomposed in slices Σ_x along the axial direction and integral indexes are calculated over each slice to characterize the mixing and combustion process observed in the simulations. The mixing process is characterized by three different integral indexes. The turbulence mixing through large scale turbulence is qualitatively assessed by circulation as shown in Eq. 1:

$$\Gamma(x) = \frac{1}{du_\infty} \iint_{\Sigma_x} \left| [\mathrm{rot}\,\mathbf{u}]_1 \right| \mathrm{d}A, \tag{1}$$

where $[\mathrm{rot}\,\mathbf{u}]_1$ is the first coordinate or x component of the vorticity vector. The description of the small

scale mixing between the hydrogen and the air is described by a mixing efficiency η_{m} that is defined by Eq. 2.

$$\eta_{\mathsf{m}}(x) = \frac{\iint\limits_{\Sigma_x} \alpha^{\mathsf{r}}_{\mathsf{H}_2} \rho u \, \mathrm{d}A}{\iint\limits_{\Sigma_x} \alpha_{\mathsf{H}_2} \rho u \, \mathrm{d}A}. \tag{2}$$

The fuel mass fraction available for the combustion $\alpha^{\mathsf{r}}_{\mathsf{H}_2}$ is a piece-wise linear function, defined by Eq. 3 as:

$$\alpha^{\mathsf{r}}_{\mathsf{H}_2} = \begin{cases} \alpha_{\mathsf{H}_2}, & \alpha_{\mathsf{H}_2} \leq \alpha^{\mathsf{st}}_{\mathsf{H}_2} \\ \left(\frac{1-\alpha_{\mathsf{H}_2}}{1-\alpha^{\mathsf{st}}_{\mathsf{H}_2}}\right) \alpha^{\mathsf{st}}_{\mathsf{H}_2}, & \alpha_{\mathsf{H}_2} > \alpha^{\mathsf{st}}_{\mathsf{H}_2} \end{cases}, \tag{3}$$

where $\alpha^{\mathsf{st}}_{\mathsf{H}_2}$ is the stoichiometric mass fraction of hydrogen and is equal to 0.0283.

This definition of the mixture efficiency is such that if the mixture in the cut-plane Σ_x is lean, η_{m} = 1 and if the mixture is purely hydrogen, η_{m} = 0. However, this index does not inform on how much air actually mixes with the fuel and defining a global equivalence ratio index can be useful to assess throttling capability. In particular with EBR, the lack of a cowl and thus of a fully physical boundary for the combustion chamber prevents the calculation of a higher bound for the available mass flow for combustion. An overall equivalence ratio ϕ is defined based on the local oxygen to hydrogen mass ratio, as shown in Eq 4:

$$\phi(\Sigma_x) = \frac{\dot{m}^*_{\mathsf{H}} / \dot{m}^*_{\mathsf{O}}}{\left(\dot{m}_{\mathsf{H}_2} / \dot{m}_{\mathsf{O}_2}\right)_{\mathsf{st}}}. \tag{4}$$

The mass flow of oxygen and hydrogen are calculated based on their atomic mass fraction in all species so that ϕ is continuous through combustion. The mass flow of oxygen is calculated only in the cells where atomic hydrogen is present. The effect of extremely lean mixture that can result from numerical diffusion is managed by only tracking a finite fraction of the integral mass flow of hydrogen injected. At each Σ_x, a constant value of the atomic mass fraction of hydrogen is found for which the integral value of the hydrogen mass flow is equal to 95% of the injected mass flow rate. The cells for which the hydrogen atomic mass fraction is lower than this calculated constant threshold are thus excluded from the integral.

Finally, a combustion efficiency is defined based on the difference of the mass flow of H_2 at a given slice of the flow Σ_x between the reacting and non-reacting case (see Eq. 5).

$$\eta_{\mathsf{b}}(x) = 1 - \frac{\left.\iint\limits_{\Sigma_x} \alpha_{\mathsf{H}_2} \rho u \, \mathrm{d}A\right|_{\text{reacting}}}{\left.\iint\limits_{\Sigma_x} \alpha_{\mathsf{H}_2} \rho u \, \mathrm{d}A\right|_{\text{non-reacting}}}. \tag{5}$$

The results showing the mixing and burning efficiencies and equivalence ratio with circulation are in Figure 5a and Figure 5b, respectively.

The injection of hydrogen in the supersonic cross-flow exhibit features very similar to that described in the scramjet literature [15]. The injection near the leading edge strongly interacts with the oblique shock wave induced by the compression ramp which displaces the boundary-layer and the shock angle to a significant degree (see Figure 6). This behaviour is also observed by holographic interferometry in the experiment [7].

There are three main phases in the mixing and combustion process. The cross-flow injection of hydrogen generates a strong flow separation around the jet and this interaction generates strong vortical structures in the flow. The normalized circulation capture this increase well and after the injection, the circulation rises by a factor of 6 compared to the no-injection conditions (see Figure 5b). The hydrogen injection results in the bulk mixing of the hydrogen and air and the mixing efficiency quickly increases up to 50%

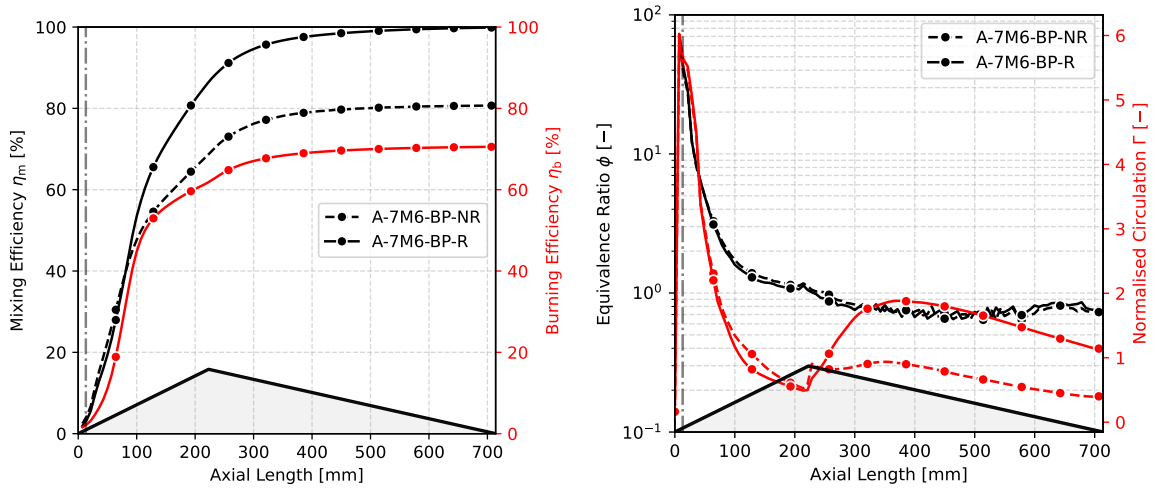

(a) Mixing and burning efficiency.

(b) Equivalence ratio and circulation.

Fig 5. Axial evolution of mixing and combustion indexes on the reference case (non-reactive and reactive).

at 100 mm (at about 0.5%/mm) downstream of the injector (see Figure 5a). However, the turbulence quickly decays and half-way through the compression surface, the circulation drops by a factor of 3, which strongly slows down the mixing process and is seen as an inflexion on the mixing efficiency evolution. The bulk mixing phase also enables the combustion and about half of the hydrogen burns in the first half of the compression surface. Within this region, the reactive and non-reactive cases have similar circulation and equivalence ratio levels.

In the second phase, which happens from the second half of the compression surface up to slightly after the turning point, the mixing efficiency keeps increasing, but at a reduced rate. The combustion efficiency slows down and from 100 mm up to 300 mm along the compression surface its efficiency increases from 50 % up to 70 % respectively (0.1 %/mm gradient). The non-reactive case differs from

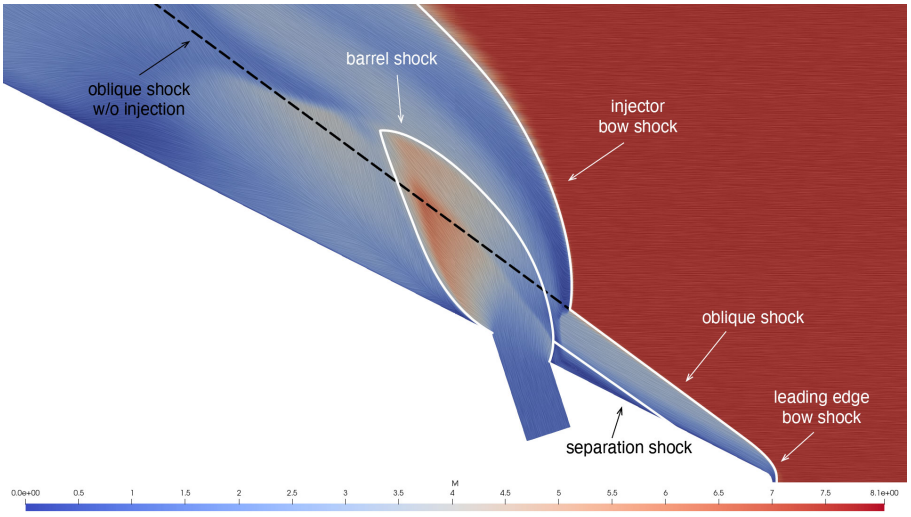

Fig 6. Mach field contours extracted from the symmetry surface for frontal (A) injector. Figure shows the injector nearfield impinged by the incoming oblique shock wave generated at the leading edge of the compression ramp. Mach contours superimposed by Line Integral Convolution (LIC), visualising the flowfield streamlines.

the reactive case. The combustion is shown to have about twice the circulation strength (see Figure 5b) compared to the non-reactive case, which is thought to explain the differences observed between both cases. From 100 mm to the turning point, the mixture is still rich (ϕ ranges 1.6 to 1.1) which might also contribute to limiting the increase rate of η_m. An overall rich mixture means that further air required for mixing needs to be entrained from outside of the jet, leading to rich pockets in the center that mix much slower that the sides of the jet. For a premixed mixture of hydrogen-air, the ignition delay is rather insensitive to the equivalence ratio [19]. In this case, the hydrogen is injected cold, which lowers the local mixture temperature. Overall, this leads to a significant increase of the ignition delay with the local equivalence ratio [19]. This could explain why even though the equivalence ratio of the mixture reaches the range where the ignition delay becomes insensitive, the combustion is still slower to occur.

In the third phase and further down the turning point, η_m in the non-reactive case stops while η_m in the reactive case eventually reaches 100% towards the second half on the expansion surface. The combustion stops shortly after the turning point. This suggests that mixing and local equivalence ratio is not responsible for combustion quenching throughout the turning point. Looking at the distribution of the temperature near the turning point (see Figure 7), one can see that despite the presence and burning of hydrogen, the temperature drops significantly due to flow expansion throughout the expansion fan. Similarly, the pressure on the expansion surface is shown to be about a factor of 8 lower compared to

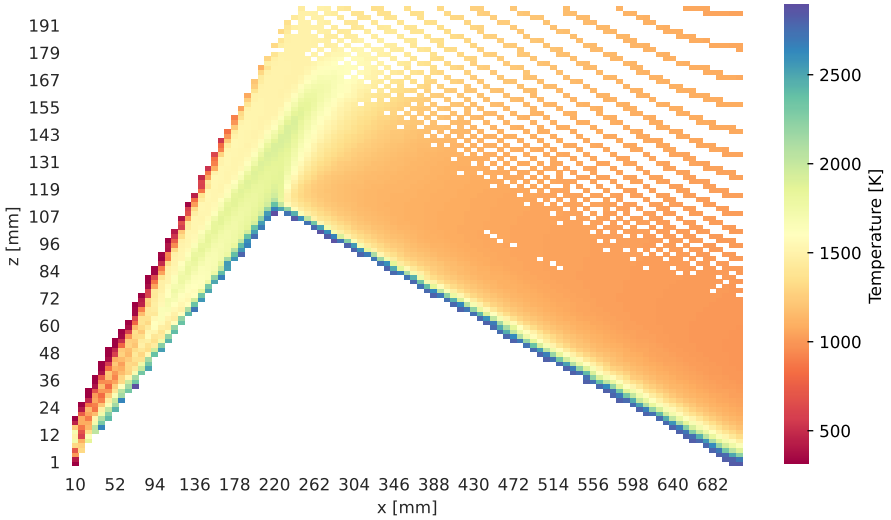

Fig 7. A 2D histogram of all the cells of the computational domain. Contours show the volume-weighted average temperature. Cells are queried such that each cell must contain traces of hydrogen species, including the radicals. The empty space is a result of both the queried result not existing in the given x and z coordinate or the fact that the underlying grid is not orthogonal.

the compression surface (see Figure 4). This temperature and pressure drop throughout the expansion fan, coupled with the fast acceleration of the flow, seems to hinder the exothermic chemical reactions [19].

4. Results

4.1. Influence of the Injector Position

The hydrogen injector is moved to two other positions downstream of the compression surface. The complexity of the jet interaction then differs based on the location of the injector and its conditions.

In configuration (A), the jet is met with a strong freestream-to-jet momentum flux, effectively impinging the injected hydrogen plume onto the compression surface, as shown in Fig. 6. The situation is different to injectors positioned further away from the leading edge, such as the mid-point injector (B) and especially the turning point injector (C) that experiences a well-developed boundary-layer. The barrel

shock of injector (A) is comparatively smaller to the barrel shocks of injectors (B) and (C) for the same conditions and the hydrogen flow on all injectors remains under-expanded for all injection pressures simulated in Table 1.

Overall, maximum post-injection peak circulation reduces with the increasing distance of the injector from the leading edge. The further the injector, the lower the circulation is, which effectively reduces the mixing efficiencies for injector (B) and (C) at the turning point. Since the turbulent decay have less time to occur, the circulation on injector (B) and (C) remains higher throughout the expansion compared to injector (A) (see Figure 8b).

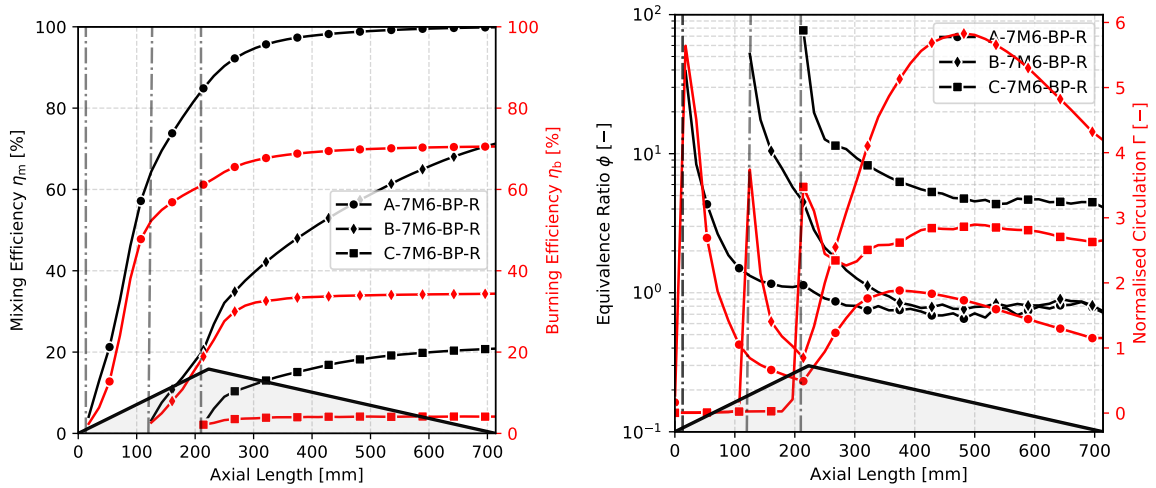

(a) Mixing and burning efficiency.

(b) Equivalence ratio and circulation.

Fig 8. Axial evolution of mixing and combustion indexes based on the injector location (reactive cases only).

In configuration (B), the evolution of mixing efficiency throughout the expansion is similar to that of configuration (A). However, the final combustion efficiency reduces almost proportionally to the injector position and stagnates at the same axial position regardless of the configuration (see Figure 8a). This reinforces the idea that the combustion is hindered more by the rapid drop in temperature and pressure throughout the expansion fan, rather than the lack of mixing. This can further be seen for configuration (C), where mixing efficiency once again increases throughout the expansion surface, while the burning is quenched.

4.2. Influence of the upstream Mach number

The upstream Mach number is increased at a constant static temperature and pressure, which increases the stagnation pressure, temperature and associated mass flux of the incoming flow. In configuration (C) and with the reference Mach number ($M = 7.6$), the mixing is slow and the combustion efficiency remains limited. The increase of the Mach number was expected to increase the amount of air available for mixing and introduce further rise in the strength of vortical structures. This is effectively what happens for injector A, where the mixing efficiency and circulation increases (see Figure 9) while the equivalence ration ϕ is decreased. In configuration (C), the increase of Mach number also reduces the equivalence ration, however contrary to the configuration (A), the circulation is reduced and so is the mixing efficiency. The overall higher post-shock temperature and compression leads to higher reaction rates and much higher combustion efficiencies at $M = 11.4$ for both injector (C) and (A) (see Figure 9a). In either case, the combustion still stops at a similar position past the expansion point, however the increase in temperature seem to increase the combustion process throughout the expansion fan.

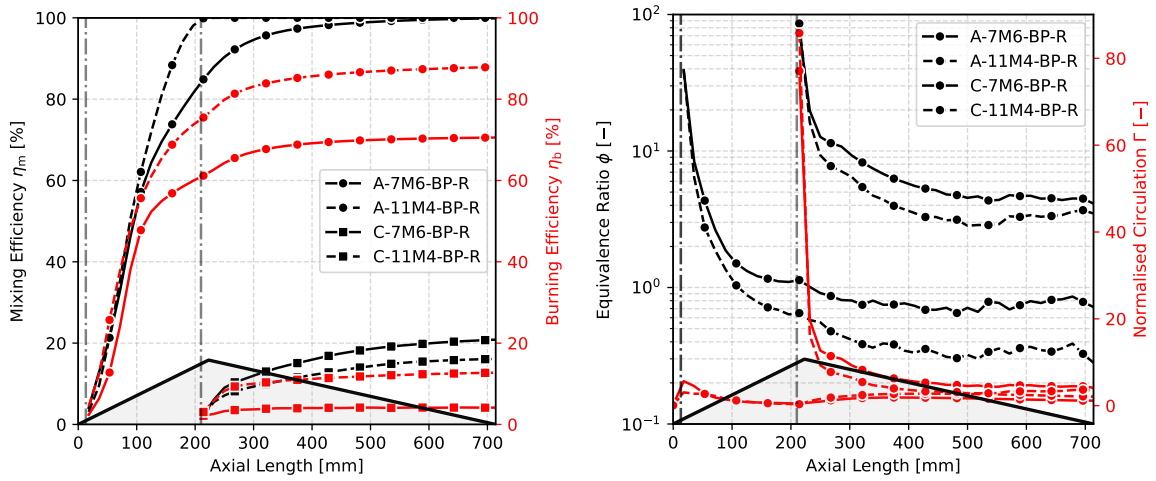

(a) Mixing and burning efficiency.

(b) Equivalence ratio and circulation.

Fig 9. Axial evolution of mixing and combustion indexes based on the free-stream Mach number (reactive only).

4.3. Influence of the fuel pressure

The fuel pressure for injector (A), was increased to 100 % of the reference case and for injector (C), was reduced to 50 % of the reference case (see Table 1). The mass flow of hydrogen is directly proportional to the hydrogen pressure. A lower injection pressure should lower the resulting equivalence ratio ϕ of the mixture. Varying the pressure also varies the momentum carried by the jet, which either increases or reduces the penetration length for an increase or a reduction of pressure, respectively. The influence of the fuel jet penetration then impacts the subsequent mixing [20].

Variation of the injection pressure was introduced to injectors (A) and (C) for the freestream conditions at $M = 11.4$. In configuration (A), the fuel pressure is doubled compared to the baseline in order to compensate for the drop in ϕ that is associated with the higher Mach number. Indeed, the distribution of equivalence ratio achieved at higher pressure is very similar to that at $M = 7.6$ for the baseline pressure. However, the associated circulation and mixing efficiency are similar than in **A-7M6-BP-R** and as a result the final combustion efficiency is of similar magnitude (63 % at 300 mm compared to 67 % in **A-7M6-BP-R**) (see Figure 10). In configuration (C), the pressure is reduced by half in order to try and reduce the resulting ϕ. However, in this case, reducing the pressure leads to a much lower circulation intensity which leads to a similar ϕ as the baseline pressure (see Figure 10). This also leads to very similar combustion efficiencies.

5. Conclusion

Three-dimensional computational simulations of an EBR combustor were performed using hydrogen injection with varying injector location and injector pressure into a Mach 7.6 and Mach 11.4 crossflow. Three injector locations are investigated, (A) 13 mm, (B) 135 mm and (C) 237 mm from the leading edge of the combustor, respectively. The injector pressure is adjusted to compensate for the increase in Mach number and to adjust the overall equivalence ratio of the hydrogen-air plum that subsequently forms. The geometry simulated is that of previous published experimental data, so that a reference case can be validated against the available experimental results.

The simulated pressure traces are a good match to the experimental measurements, Hhowever the specific impulse derived from the pressure yields very different values. The discrepancies are thought to be associated with pressure side-relief occurring in the experiments, where lower pressure is also seen to affect the combustion process. In the numerical simulation of the reference case, it is shown that mixing and combustion occurs very quickly downstream of the injector and that more than 50% of the fuel is burnt on the first half of the compression surface. The overall ϕ in this case is slightly rich

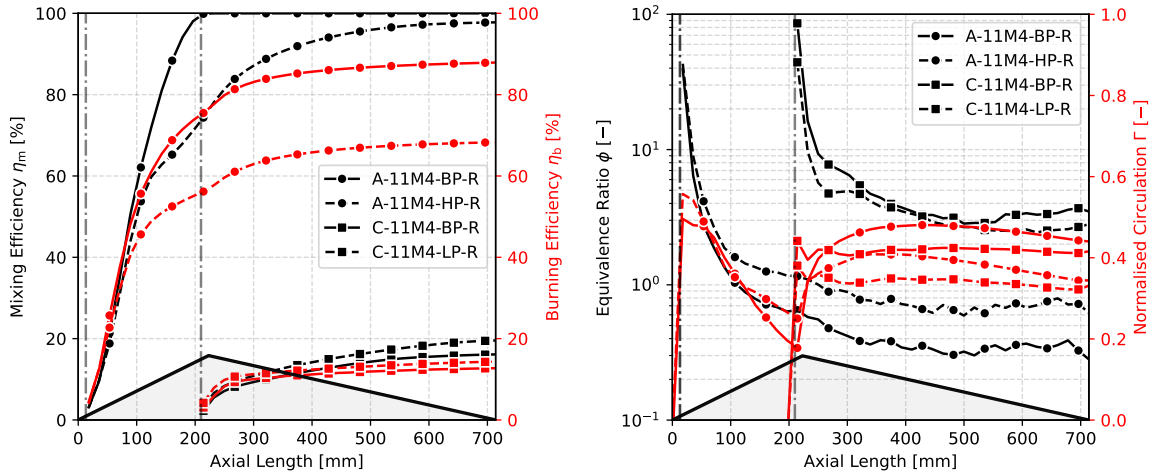

(a) Mixing and burning efficiency.

(b) Equivalence ratio and circulation.

Fig 10. Axial evolution of mixing and combustion indexes on the injector pressure (reactive only).

near the turning point and although the mixing efficiency reaches 100% on the expansion surface, the combustion is quenched by the expansion fan. This quenching occurs at a similar position for all cases and is thought to be mainly driven by the drop of temperature and pressure and rather independent of mixing.

References

1. Smart MK. How Much Compression Should a Scramjet Inlet Do? AIAA Journal 2012;50:610–9.
2. Smart MK. Experimental Testing of a Hypersonic Inlet with Rectangular-to-Elliptical Shape Transition. Journal of Propulsion and Power 2001;17:276–83.
3. Larsson J, Laurence S, Bermejo-Moreno I, Bodart J, Karl S, and Vicquelin R. Incipient Thermal Choking and Stable Shock-Train Formation in the Heat-Release Region of a Scramjet Combustor. Part II: Large Eddy Simulations. Combustion and Flame 2015;162:907–20.
4. Heiser W, Pratt D, Daley D, and Mehta U. Hypersonic Airbreathing Propulsion. AIAA, 1994.
5. Broadbent EG. An Exact Numerical Method of Calculating Inviscid Heated Flows in Two Dimensions with an Example of Duct Flow. Ingenieur-Archiv 1971;40:14–28.
6. Broadbent EG. Flows with Heat Addition. Progress in Aerospace Sciences 1976;17:93–107.
7. Coras S and Paull A. Experiments on External Combustion with Leading Edge Fuel-Injection in Hypersonic Flow. In: *14th AIAA/AHI Space Planes and Hypersonic Systems and Technologies Conference*. International Space Planes and Hypersonic Systems and Technologies Conferences. American Institute of Aeronautics and Astronautics, 2006.
8. Pudsey AS, Wheatley V, and Boyce RR. Behavior of Multiple-Jet Interactions in a Hypersonic Boundary Layer. Journal of Propulsion and Power 2014;31:144–55.
9. Billig FS. A Study of Combustion in Supersonic Streams. PhD thesis. 1964.
10. Billig FS. External Burning in Supersonic Streams. Tech. rep. John Hopkins University, 1967.
11. Küchemann D. Hypersonic Aircraft and their Aerodynamic Problems. Prog. Aerosp. Sci. 1965;6:271–353.
12. Dorrington GE. Propulsive Efficiency of Hypersonic External Burning. Journal of Spacecraft and Rockets 2000;37:144–7.
13. Jones JR and Christo FC. Numerical Analysis of External Supersonic Combustion of Hydrogen and Ethylene. In: 2007.
14. R. MF. Two-Equation Eddy-Viscosity Turbulence Models for Engineering Applications. AIAA Journal, Vol. 32, No. 8, August 1994 2002.

15. Pudsey AS, Boyce RR, and Wheatley V. Hypersonic Viscous Drag Reduction via Multiporthole Injector Arrays. J. Propul. Power 2013;29:1087–96.
16. Jachimowski CJ. An Analysis of Combustion Studies in Shock Expansion Tunnels and Reflected Shock Tunnels. Tech. rep. NASA, 1992.
17. Celik IB, Ghia U, Roache PJ, Freitas CJ, Coleman H, and Raad PE. Procedure for Estimation and Reporting of Uncertainty Due to Discretization in CFD Applications. Journal of Fluids Engineering 2008;130.
18. Coras SJ. Forebody Combustion Experiments on an Unducted Scramjet. University of Queensland, 2011. URL: https://espace.library.uq.edu.au/view/UQ:261604.
19. Huber PW, Schexnayder CJ, and McClinton CR. Criteria for Self-Ignition of Supersonic Hydrogen-Air Mixtures. 1979:60.
20. Pudsey AS and Boyce RR. Numerical Investigation of Transverse Jets Through Multiport Injector Arrays in a Supersonic Crossflow. Journal of Propulsion and Power 2010;26:1225–36.